

A Low-loss and Lightweight Magnetic Material for Electrical Machinery

Farzad Ahmadi^{1*}, Yilmaz Sozer², Michael J. Donahue³, Igor Tsukerman²

¹ Department of Electrical and Computer Engineering, Youngstown State University, Youngstown, OH, 44555 USA

² Department of Electrical and Computer Engineering, University of Akron, Akron, OH, 44325-3904 USA

³ Applied and Computational Mathematics Division, National Institute of Standards and Technology, Gaithersburg, MD 20899-8910, USA

* E-mail: fahmadi@ysu.edu

Abstract: A low-loss and lightweight core material, with applications in electrical machinery, is made of highly packed and insulated magnetic microwires (MWs). These MWs are aligned in such a way as to guide the flux in the rotor/stator, with the ultimate goal of increasing efficiency and substantially reducing core losses. Commercial Fe₆₀Ni₂₉Co₁₇-based MWs with a 127 μm diameter and a 33 μm insulation coating are utilized. The magnetic measurements of the fabricated sample demonstrate high permeability and low core loss in a wide range of frequencies. To prove the utility of this type of material, we used it in the rotor core of a prototype 25 Watt three-phase synchronous reluctance machine (SyncRM). The core is lighter, and the losses are significantly lower than in conventional core materials under the same torque density.

1 Introduction

Since rare-earth Permanent Magnet (PM) materials are expensive and scarce, Synchronous Reluctance Machines (SyncRMs) [1] have emerged as a promising alternative to PM machines for traction applications [2–4]. SyncRMs have a simple control drive, no rotor slip losses, inherently smooth and quiet rotation, better efficiency and torque density but a lower power factor in comparison with Induction Motors (IM) [5, 6].

There are two general types of SyncRM: transversely laminated anisotropic and axially laminated anisotropic [6]. The latter have higher torque density, a higher power factor, and higher efficiency due to a high saliency ratio (i. e. the ratio of the direct axis inductance to the quadrature axis inductance). On the downside, axially laminated anisotropic machines require a more complicated assembly process.

Silicon steel is widely used in electrical machines as a soft magnetic material because of its high flux density and low cost. However, alternative new materials with lower loss than in silicon steel are highly desirable.

The core loss consists of hysteresis loss P_{hys} , eddy current loss P_{edd} , and excess loss P_{exc} . The hysteresis loss stems from the domain wall motion [7, 8]. At moderate and low frequencies of sinusoidal magnetic field excitation the eddy current loss per unit volume is $P_{\text{edd}} = (\pi D f B_{\text{max}})^2 / (\rho \beta)$, where ρ is the resistivity, D is the thickness for laminations or diameter for cylinders and spheres, and β is a geometrical factor equal to 6, 16, and 20 for laminations, cylinders and spheres, respectively [9]. To substantially reduce the eddy current loss, very thin laminations are required, which significantly increases the cost.

Hysteresis is the main loss mechanism at low frequencies. However, it is known [10–14] that when the grain size increases, the hysteresis loss decreases ($P_{\text{hys}} \propto w^{-1}$, where w is the grain size). For a fixed material dimension, when the grain size increases, the number of grain boundaries decreases. This means less external field is required to align the domains and hence the hysteresis loss decreases. The grain boundary is the source of magnetic charges and consequently the demagnetizing field. This internal field impedes the domain wall movement [15]. Therefore, there is an optimal grain size for which the total loss is minimized – typically in the range of 100 μm to 200 μm for grains with a low to medium Si content [10, 16]. For grains with a high Si content (i.e. higher resistivity) the optimum grain size increases [14].

In recent years, nanocrystalline soft magnetic alloys have emerged as promising alternative materials, with low core loss, low magnetostriction, good thermal stability, and high permeability [17–21]. Of all nanocrystalline soft magnetic alloys, amorphous Co-based and Fe-based nanocrystalline materials exhibit superior characteristics [18, 19, 22]. FeNiCo has high saturation magnetization (2.1 T), low coercivity, low magnetostriction, and high permeability even at high frequencies [23, 24]. Herzer [18] proposed a Fe₇₄Cu₁Nb₃Si_xB_{x-7} alloy as a soft magnetic material with high saturation magnetization, high permeability, good high frequency behavior, low-losses, and good thermal stability. Recently, Suzuki *et al.* [25] proposed a new magnetic material based on nanocrystalline Fe₈₅B₁₃Ni₂. This material has high saturation magnetization of 1.9 T and low core losses, with the coercivity field 4.6 Am⁻¹. Similar results are obtained for FeNb [26] and FeCo-based [27] alloys.

In rotating electrical machines, the core material experiences a high temperature and a high magnetic field. That is where strain responses to temperature and the magnetic field, known as thermal expansion and magnetostriction, respectively, play a key role. Any strain (shrink or stretch) of the core material can strongly affect the performance of electrical machines [28–31]. For example, if the rotor/stator core material stretches, then the air gap narrows and consequently the torque ripple, noise and vibration increase. Therefore, ideally the material should have low thermal expansion and magnetostriction to minimize the stress effects.

Recently, a SyncRM based on a dual-phase material was proposed [32]. In such a material, the bridge and center post regions are made of non-magnetic materials and the rest of the lamination is magnetic. The SyncRM made of a dual-phase material exhibited a higher power density and constant power speed ratio in comparison with the conventional one.

The objective of our work is to demonstrate the feasibility of the commercial nanocrystalline materials and their applications in the design of low-loss electrical machines. The composite provides an array of microscale magnetic flux paths. The MW-based material offers very low core losses and a high permeability over a wide range of magnitudes of applied fields.

The paper is organized as follows. The experimental setup and measurement results of a MW-based material are presented in sections 2 and 3, respectively. The performance of a SyncRM with the MW-based material is simulated and compared with that of a

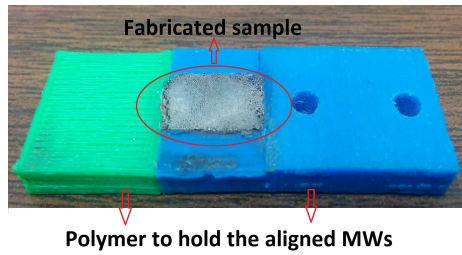


Fig. 1: A sample based on aligned $\text{Fe}_{\text{bal}}\text{Ni}_{29}\text{Co}_{17}$ MWs. The samples width, length, and height are 6.5 mm, 10.5 mm, and 4.5 mm, respectively.

similar conventional material in section 4. Finally, a summary and conclusion are given.

2 Experimental setup

We chose to work with the $\text{Fe}_{\text{bal}}\text{Ni}_{29}\text{Co}_{17}$ alloy because it is available as commercial wires. (There are also other elements in the chemical composition with less than 1% of the alloy weight.) The Ni and Co contents are 29% and 17%, respectively. The 53% remainder of the alloy weight, which is presented as abbreviation of balance, is made of Fe.

We recently developed a new technique to align ferromagnetic MWs in either straight or curved shape, suitable for the rotor and stator geometry. The commercial MWs have a 33 mm layer of a polyimide coating, which electrically insulates the bundled wires. The melting temperature of polyimide is 240 °C, which is high enough for a core material in rotating electrical machines.

Two samples based on the MWs are fabricated to measure their magnetic properties. To fabricate the composite, we made polymer-based sample casts using 3D printing technology. To ease the handling process of such thin wires, we wrapped the MWs around polymer-based plates with the same length as the samples. Then, we formed bundles of MWs after making a cut at each end of the plate. We later placed the bundles into the casts where a low-viscosity adhesive super bonder serves as a non-magnetic matrix.

A fabricated sample of highly packed MWs made of $\text{Fe}_{\text{bal}}\text{Ni}_{29}\text{Co}_{17}$ is shown in figure 1. The diameter, inter-wire distance, and length of the MWs are 127 μm , 155 μm , and 4.5 mm, respectively. The width, length, and height of the samples are 6.5 mm, 10.5 mm, and 4.5 mm, respectively. The weight, wire volume fill factor, and density are 1.4 g, 0.38, and 4600 kg/m^3 , respectively.

The method introduced by Thottuvelil *et al.* [33] is used to measure the magnetic characteristics of the samples. Based on this method, the magnetic field intensity H and the magnetic flux density B are measured by the primary winding current and the voltage across the secondary winding, respectively. The method is sensitive to the phase discrepancy between the measured current and voltage at high frequencies, which causes an error. However, since the operating frequency in our application is very low, this technique is utilized here to measure the core loss and the hysteresis loop at different frequencies.

The experimental setup is illustrated in figure 2. Two samples based on the proposed composite are fabricated. The samples are sandwiched between two nanocrystalline C cores with primary and secondary windings. The cross-sectional area, inner and outer diameters of the C cores are 10 mm \times 6 mm, 45 mm, and 55 mm, respectively. The nanocrystalline C core data sheet is shown in table 1.

3 Measurement results of a MW-based Material

To properly characterize a material, the hysteresis loop at different frequencies is needed. Two different measurement cases are considered to separately derive the magnetic properties for the testing C

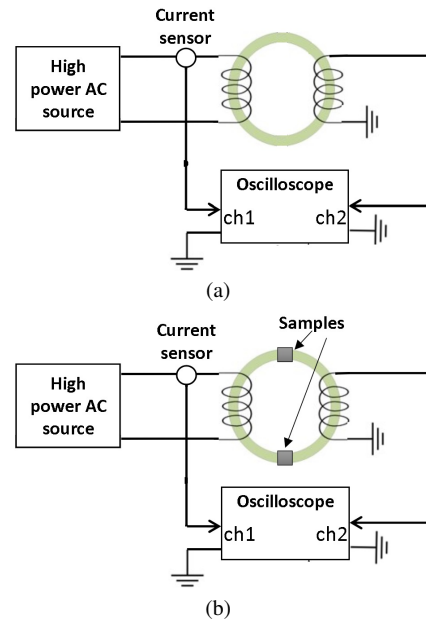


Fig. 2: Schematic of the experiment setup to measure the hysteresis loop and core loss of the testing C cores a) without, and b) with the samples. c) Experimental setup.

cores and samples. In the first case, the hysteresis and core loss are measured for only the testing C cores without the samples between them. In the second case, the hysteresis and core loss are measured when the samples are placed between the testing C cores. Finally, the core losses of the testing C cores with and without samples are subtracted to obtain the samples losses.

First, we need to characterize the properties of the testing C cores themselves, without the samples. To this end, two testing C cores are

Table 1 Nanocrystalline cores data sheet [34]

Parameter	Experimental condition	value
Saturation induction (T)		1.25
Residual induction (T)	20 kHz	<0.2
Core loss (W/kg)	20 kHz, 0.2 T	<3.4
Core loss (W/kg)	20 kHz, 0.5 T	<3
Core loss (W/kg)	50 kHz, 0.3 T	<4
Relative permeability	20 kHz	>20 000
Coercivity (A/m)	20 kHz	<1.6
Saturation magnetostriction		$2 \cdot 10^{-6}$
Resistivity ($\mu\Omega \cdot \text{cm}$)		80
Curie temperature ($^{\circ}\text{C}$)		570
Stacking factor		0.7

placed in direct contact to form a toroidal core. A sinusoidal wave is applied to the primary winding of the C cores using a high power AC source. From Ampere's law, the testing C cores magnetic field in figure 2(a) is

$$H_{C\text{-core}}(t) = \frac{N_p i_p(t)}{l_{C\text{-core}}} \quad (1)$$

where N_p is the number of primary turns, i_p is the primary current, and $l_{C\text{-core}}$ is the effective length of the toroidal. Using Faraday's law, $v_s = N_s d_t \phi$, we get the average flux density in the cores

$$B(t) = \frac{1}{N_s A_{\text{eff}}} \int_0^t v_s(\tau) d\tau \quad (2)$$

where N_s is the number of secondary turns, A_{eff} is the effective cross-section area of the C core, and v_s is the secondary voltage. For a uniform flux density B throughout the entire volume, the hysteresis energy loss is

$$W_m = v \oint H dB \quad (3)$$

where v is the effective volume of the core. Moreover, at an operating frequency f , there are f hysteresis loops per second, so by substituting (1) and (2) into (3), one expresses the core power loss in the testing C cores as

$$\begin{aligned} P_{C\text{-core}} &= v f \int_0^T H_{C\text{-core}}(t) \frac{dB(t)}{dt} dt \\ &= \frac{1}{T} \int_0^T v_p(t) i_p(t) dt \quad (4) \end{aligned}$$

where T is the time cycle and v_p is the primary voltage. The measurements are performed using an Op-Amp based integrator and an analog multiplier chip.

From the hysteresis curve of the testing C cores, the relative permeability is

$$\mu_{C\text{-core}} = \frac{B_{C\text{-core}}}{\mu_0 H_{C\text{-core}}} \quad (5)$$

Note that the C cores and samples have the same average cross-section area. However, in the samples, the flux density is averaged over the whole bunch of wires, including the bonding substance.

When the samples are placed between the C cores as in figure 2(b), we solve the simple magnetic circuit using Ampere's law

$$\begin{aligned} N_p i_p &= H_{C\text{-core}} L_{C\text{-core}} + H_{\text{sample}} L_{\text{sample}} = \\ &= \frac{L_{C\text{-core}}}{\mu_0 \mu_{C\text{-core}}} B_{C\text{-core}} + \frac{2L_{\text{sample}}}{\mu_0 \mu_{\text{sample}}} B_{\text{sample}} \quad (6) \end{aligned}$$

Here L_{sample} is the sample length, $L_{C\text{-core}}$ is the effective length of the C cores, B_{sample} is the sample magnetic field density, $B_{C\text{-core}}$ is the core magnetic field density. Using the magnetic flux continuity condition at the interface between C cores and samples, the relative permeability of the new composite is

$$\mu_{\text{sample}} = \frac{2L_{\text{sample}} B_{\text{sample}}}{\mu_0 N_p i_p - \frac{B_{\text{sample}} L_{C\text{-core}}}{\mu_{C\text{-core}}}} \quad (7)$$

The measured hysteresis loops are shown in figure 3(a) for three different frequencies: 250 Hz, 500 Hz, and 1 kHz. In this figure, the black curve shows the relative permeability at 1 kHz for the C cores, with saturation at 1.23 T (very close to 1.25 T given in the data sheet, Table 1). Furthermore, the red, purple, and green hysteresis loops are obtained when the samples are sandwiched between the C cores at 250 Hz, 500 Hz, and 1 kHz, respectively. As seen, the hysteresis loops for all three frequencies are quite similar, with a high saturation magnetization of 1.1 T and low hysteresis loss for all three frequencies. However, in comparison with the cores (black

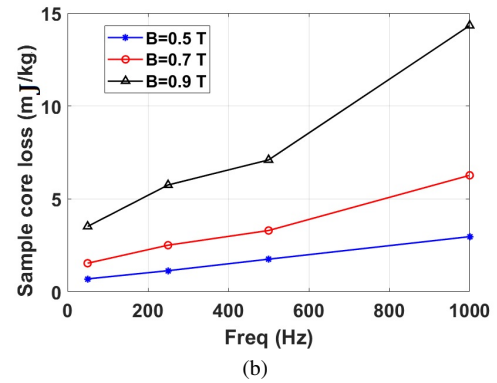
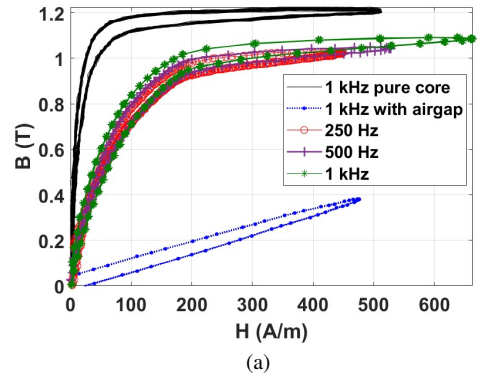


Fig. 3: a) The measured hysteresis loops at different frequencies. The blue and black curves correspond to the C cores at 1000 Hz without and with a 4.5 mm air gap between them, respectively. The red, purple, green curves correspond to samples sandwiched between C cores at 250 Hz, 500 Hz, and 1 kHz. b) Losses in the samples per frequency (P_{sample}/f) as a function of frequency at three different flux densities 0.5 T (asterisks), 0.7 T (circles), and 0.9 T (triangles).

curve), the samples show an 8% lower saturation magnetization and require a higher magnetic field to saturate. A linear blue curve is obtained when there is a 4 mm air gap (whose width is equal to the height of the samples) between the C cores at 1 kHz (see figure 3(a)).

Figure 3(b) shows the sample losses per frequency ($P_{\text{sample}}/f = K_{\text{hys}} B^{1.6} + K_{\text{edd}} f B^2 + K_{\text{exc}} f^{0.5} B^{1.5}$) as a function of frequency at three different flux densities: 0.5 T, 0.7 T, and 0.9 T. Clearly, the loss increases with the flux density and frequency. At frequencies below 500 Hz the losses increase slightly when the frequency increases; the hysteresis loss is dominant. However, when the frequency doubles from 500 Hz to 1000 Hz, the losses are doubled in all three cases. This indicates that the eddy current losses are considerable.

In Table 2 the core losses of the conventional M19-grade material are compared with the proposed MW-based material at different frequencies and magnetic fields. The M19-grade lamination thickness is 0.36 mm. The MW-based material shows low core losses at all frequencies and fields. For example, at 50 Hz, the losses in M19-grade are 0.31 W/kg and 0.83 W/kg, as compared with 0.03 W/kg and 0.17 W/kg for the MW-based material at 0.5 T and 0.9 T, respectively. Also, at 1000 Hz, the MW-based material has one sixth core loss at 0.5 T compared with the M19-grade. The low loss at high frequencies makes $\text{Fe}_{\text{bal}}\text{Ni}_{29}\text{Co}_{17}$ MW-based composite a promising material in electrical machines for high speed applications. Moreover, the MW-based material is almost 40% lighter than conventional silicon steel, which is a remarkable reduction.

The MW diameters are in the range of the optimal grain size, minimizing core losses as a trade-off between hysteresis and eddy current losses [10, 16].

Since the hysteresis loops for the sample at all three frequencies 250 Hz, 500 Hz and 1 kHz are quite similar, we derive the permeability only for the 1 kHz case (figure 4). In this figure, the asterisks and circles show the relative permeability at 1 kHz for the C cores and the samples, respectively. The relative permeabilities of the samples are high (around 1000) in a wide range of external fields. These results suggest that MW-based materials can be used as an alternative in rotating electrical machines, where high permeability and low loss are highly desirable.

4 Simulation results of a MW-based SyncRM

The MWs create the desired magnetic flux paths for the flux generated by the stator. The flux passes through the rotor, and torque is generated through the magnetic reluctance phenomenon. Finite element analysis* is used to study a SyncRM for rotor core material made of $Fe_{bal}Ni_{29}Co_{17}$. Figure 5 shows the simulation model of a MW-based SyncRM. Parameters used in the simulation are presented in table 3. The numerical setup is discussed in appendix 7.1.

The rotor core is made of the MW-based material whose magnetic properties are given in section 3. There is a flux barrier between the MWs. The thin wires guide the flux in their direction of alignment. A low permeability perpendicular to the MWs is created because of the proposed structure. The flux barriers and the aligned MWs provide an anisotropic material in the rotor which causes a reluctance torque. The induced phase voltages are shown in figure 6. The obtained torque is 0.16 Nm, with a ripple of 37%.

Figure 7 shows the rotor losses of the SyncRM based on the MW material. The average total (black curve), hysteresis (red curve), eddy current (blue curve), and excess (purple curve) losses are 11.5 mW, 7.8 mW, 3.5 mW, and 0.2 mW, respectively. The excess

*Commercial software ANSYS Maxwell is used in this paper to simulate the SyncRM. Such identification is not intended to imply recommendation or endorsement by the National Institute of Standards and Technology, nor is it intended to imply that the software identified is necessarily the best available for the purpose.

Table 2 Core loss comparison between M19-grade [35] and the MW-based material at different frequencies. M19-grade is silicon steel with lamination thickness 0.36 mm

Freq (Hz)	M19-grade (W/kg) [35]	MW-based material (W/kg)
50	0.31 (@0.5 T), 0.83 (@0.9 T)	0.03 (@0.5 T), 0.17 (@0.9 T)
200	2.5 (@0.5 T), 8.5 (@0.9 T)	0.28 (@0.5 T), 1.43 (@0.9 T)
500	9.4 (@0.5 T), 26.5 (@0.9 T)	0.88 (@0.5 T), 3.53 (@0.9 T)
1000	18.9 (@0.5 T), 58.4 (@0.9 T)	2.97 (@0.5 T), 14.33 (@0.9 T)

Table 3 Parameters used in the SyncRM numerical simulation

Parameter	value
Number of phases	3
Number of poles	4
Number of slots	12
Stator outer diameters	41.6 mm
Rotor outer diameters	40.6 mm
Air gap length	0.5 mm
Stack length	35 mm
Rated rotational speed	157 rad/s
Rated output power	25 W
Line voltage	200 V
Frequency	50 Hz
Line current	0.2 A
segment thickness	0.48 mm
barriers thickness	0.12 mm
Number of segments	19
Stator material	M19-grade

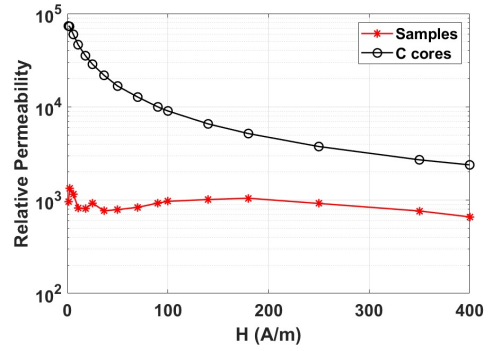


Fig. 4: Relative permeability calculated from the measured hysteresis curves (see figure 3). Black circles: C cores; red stars: samples. Frequency 1000 Hz.

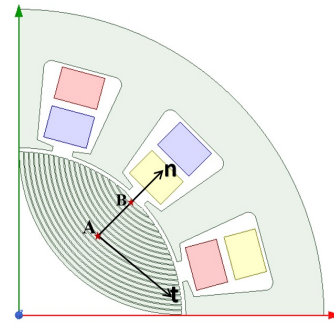


Fig. 5: 2D representation of a 25 Watt SyncRM. Parameters used in the simulation are presented in table 3. The strips are MWs. To consider the MWs insulation coating, flux barriers are introduced artificially between the MWs.

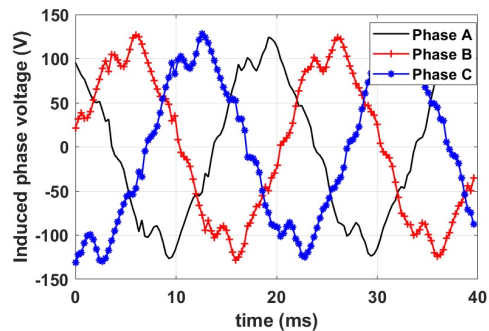


Fig. 6: Induced phase voltages of the MW-based SyncRM. The frequency is 50 Hz.

loss obtained from (9) is very small. The core loss calculation in the numerical analysis is explained in appendix 7.2.

The TLA type rotor is the most popular one in SyncRM. Therefore, a conventional TLA type rotor is compared with the proposed rotor. The rotor in figure 5 is replaced with a TLA type rotor based on the M19-grade material as shown in figure 8. The rotor dimensions are illustrated in table 4. The same stator is used in both conventional and new machine. However, a 12% higher stator current is applied in the conventional SyncRM to obtain the same torque compared with the proposed motor. That is because the ribs and bridges considerably reduce the saliency ratio in the conventional TLA type rotor. The induced phase voltages are shown in figure 9. The obtained torque ripple is 29%. The average total (black curve), hysteresis (red curve), eddy current (blue curve), and excess (purple curve) losses are 128 mW, 74 mW, 42 mW, and 4 mW, respectively, as demonstrated in figure 10. As seen, under the same torque, the loss is 11

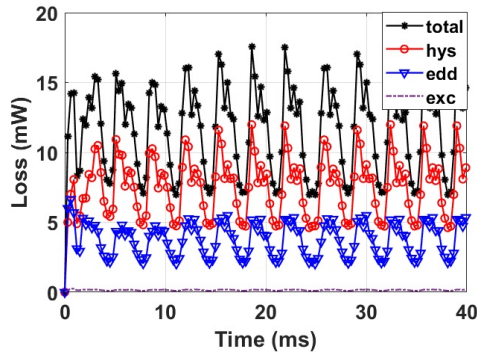


Fig. 7: Numerical results of the total core loss (black curve), hysteresis (red curve), eddy current (blue curve), and excess (purple curve) losses in a 25 Watt SyncRM rotor based on $Fe_{ba1}Ni_{29}Co_{17}$ material. The frequency is 50 Hz.

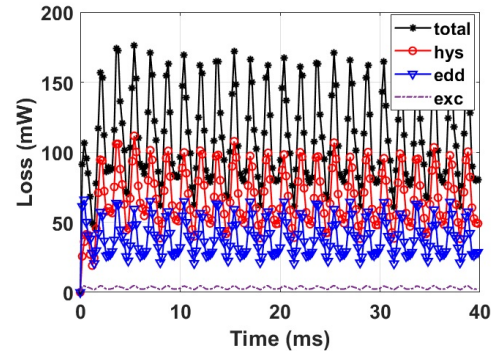


Fig. 10: Numerical results of the total loss (black curve), hysteresis (red curve), eddy current (blue curve), and excess (purple curve) losses of the conventional SyncRM. The frequency is 50 Hz.

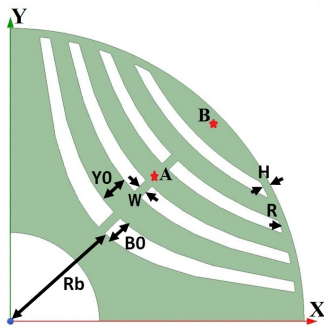


Fig. 8: 2D representation of a conventional TLA type SyncRM based on M19-grade. The rotor dimensions are shown in table 4.

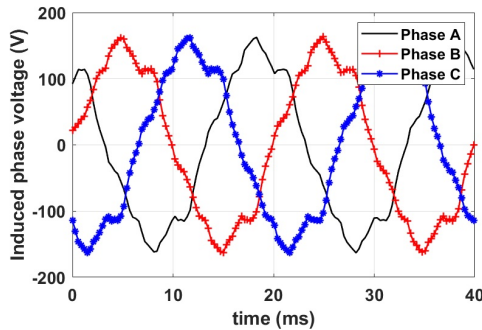


Fig. 9: Induced phase voltages of the conventional SyncRM. The frequency is 50 Hz.

times higher in the conventional rotor compared to the proposed rotor.

The saliency ratio, power factor, and power density are shown in table 5. (the stator resistance is neglected). The weights and dimensions of materials are scaled up to calculate the power density of the rotors. The proposed rotor is highly anisotropic and eliminates the tangential and radial ribs. The high numbers of microscale flux paths in the new rotor provide a higher saliency ratio and a higher power factor compared with the conventional SyncRM. The reluctance torque depends on the saliency ratio and is directly related to the magnetizing inductances. Consequently, the MW-based rotor shows a higher reluctance torque per given current, while greatly decreasing the core loss. Since, the MW-based rotor is lighter and requires a lower current for the same torque, it provides a higher power density compared with the conventional rotor.

The core loss distributions of the MW-based and conventional SyncRM rotors are shown in figures 11(a) and 11(b), respectively.

The MW-based rotor has high losses at the outer segments of the rotor and at both ends of the MWs. On the other hand, the conventional SyncRM rotor has high loss in a large part of the rotor. Figure 11 shows that the proposed rotor has lower core loss compared with the conventional TLA type rotor.

The loci of the flux density, in the tangential and normal plane to the rotor segments, provide an insight into the rotor core loss due to the rotational and DC components of the flux density. Figures 12(a) and 12(b) show the loci of the flux density at the rotor's middle segment (point A in figures 5 and 8) and outer segment (point B in figures 5 and 8), respectively. The dq transformation is used to plot the fluxes at points A and B. The results demonstrate the presence of rotational magnetic flux densities. For the MW-based rotor, both figures present large and small DC components for B_t and B_n , respectively, since the MWs are highly anisotropic. The large B_n for conventional SyncRM in figure 12(a) is due to the q-axis flux linkage caused by the radial ribs. Higher magnitudes of flux densities for both the tangential and normal components are observed in the conventional rotor compared to the magnitudes of B_t and B_n in the MW-based rotor. The higher magnitudes of flux densities with large DC components in the conventional rotor compared to the MW-based rotor result in a higher core loss.

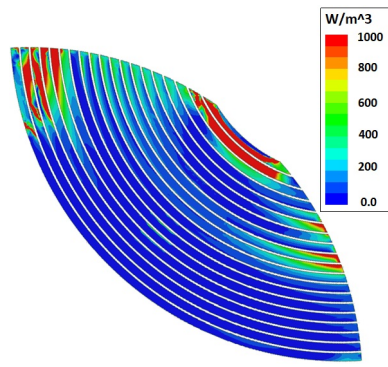
Table 6 exhibits the performance of the proposed and conventional SyncRM at three different speeds. The MW-based SyncRM

Table 4 Dimensions of the conventional SyncRM rotor used for numerical simulation. Refer to figure 8 for the parameter definitions

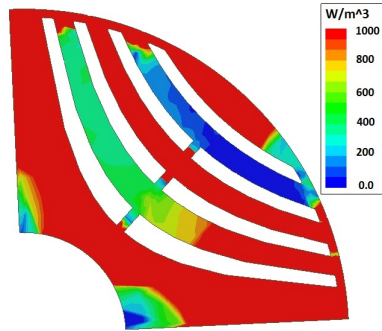
Parameter	value
Number of phases	3
Number of poles	4
Number of barriers	4
Rotor outer diameters	40.6 mm
Air gap length	0.5 mm
Stack length	35 mm
Bridge thickness, H	0.5 mm
Rib width, W	0.6 mm
Barrier bottom minimum radius, Rb	8.9 mm
Barrier bottom thickness, B0	1.5 mm
Barrier fillet radius, R	0.1 mm
Yoke bottom thickness, Y0	2 mm
Rotor material	M19-grade

Table 5 Saliency ratio, power factor, and power density of the conventional and MW-based SyncRM.

Motor	saliency ratio	power factor	power density (W/kg)
Conv. SyncRM	2.62	0.43	65.5
MW-based SyncRM	6.3	0.63	91

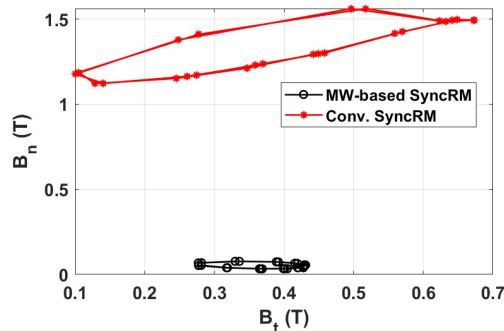


(a)

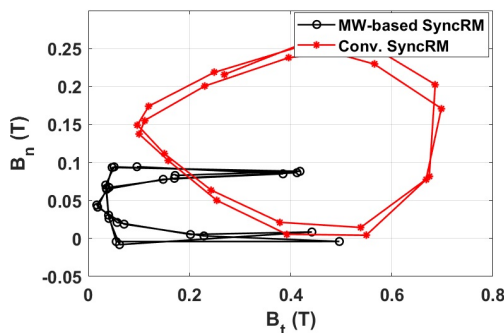


(b)

Fig. 11: Core loss distribution in the a) MW-based rotor and b) conventional SyncRM rotor.



(a)



(b)

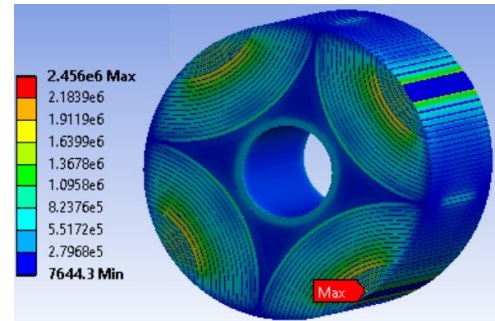
Fig. 12: Loci of the flux density (B_n vs B_t) at a) the middle segment of the MW-based and conventional rotors (point A in figure 5 and 8) and b) the outer segment of the MW-based and conventional rotors (point B in figure 5 and 8).

Table 6 Torque and losses at different speed for both the proposed SyncRM and conventional SyncRM.

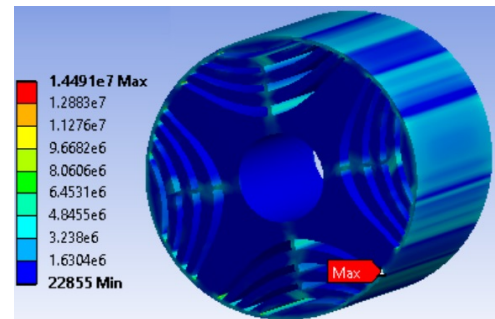
Type of SyncRM	Speed (rpm)	Torque (mNm)	rotor loss (mW)	stator loss (mW)
Proposed	1500	160	11.5	349
Conventional	1500	160	128	382
Proposed	4500	55	28	400
Conventional	4500	54	260	450
Proposed	6000	40	50	500
Conventional	6000	38	500	650

Table 7 Mechanical properties of the materials.

Material	Tensile Strength (MPa)	Yield Strength (MPa)	Young's Modulus (GPa)	Poisson's Ratio	Density (kg/m^3)
M19	503	344	210	0.31	7650
$\text{Fe}_{\text{bal}}\text{Ni}_{29}\text{Co}_{17}$	518	276	200	0.3	8359
Polyimide	231	150	2.5	0.34	1400



(a)



(b)

Fig. 13: Von Mises stress distribution in the a) MW-based, b) conventional rotors at 6000 rpm.

presents significantly lower core loss at all three different speeds compared to the conventional SyncRM.

To demonstrate the mechanical integrity of the proposed rotor, von Mises stress analyses of both rotors at 6000 rpm are shown in figure 13. The mechanical properties of the materials are presented in table 7. Maximum stresses of the proposed and conventional rotors are 2.45 Mpa and 14.49 MPa, respectively. Polyimide has much lower Young's modulus compared to $\text{Fe}_{\text{bal}}\text{Ni}_{29}\text{Co}_{17}$ and therefore shows much lower stress. However, the tangential and radial ribs in the conventional SyncRM are subject to high stress.

5 Conclusion

The objective of this work is to provide a lightweight and low loss material for the cores of electric machines. The Fe-based composite

contains microscale magnetic flux paths and exhibits high permeability and low loss over a wide frequency range. The measured core loss for the MW-based material is significantly lower than that of the conventional silicon steel. The composite is modeled in the rotor core of a prototype 25 W three-phase SyncRM. Numerical simulations show that under the same torque density, the MW-based rotor presents significantly lower core loss compared with a conventional SyncRM rotor. Furthermore, the fluxes at different positions in the rotor segments demonstrate the presence of rotational flux density, which causes additional core loss in the array of MWs. The proposed technology eliminates the bridges and center posts, while maintaining the required mechanical rigidity. This provides a higher stator and rotor diameter with reduced axial length for higher torque densities. Low loss at high frequencies, lightweight, and mechanical robustness make the MW-based material a potential candidate for high speed electrical machines.

Acknowledgment

The authors thank Dr. Robert Shull for discussions and gratefully acknowledge the use of the computational resources of Ohio Supercomputer Center [36]. The research of YS was supported in part by fellowships from ABB US Corporate Research and by the State of Ohio Innovation Platform Program. The work of FA and IT was supported in part by the US National Science Foundation Grant DMS-1620112 and by a fellowship from ABB US Corporate Research.

6 References

- Kostko, J.K.: 'Polyphase reaction synchronous motors', *Journal Amer Inst Elect Engrs*, 1923, **42**, (11), pp. 1162–1168
- Ferrari, M., Bianchi, N., Doria, A., Fornasiero, E.: 'Design of synchronous reluctance motor for hybrid electric vehicles', *IEEE Trans Ind Appl*, 2015, **51**, (4), pp. 3030–3040
- Bianchi, N., Bolognani, S., Carraro, E., Castiello, M., Fornasiero, E.: 'Electric vehicle traction based on synchronous reluctance motors', *IEEE Trans Ind Appl*, 2016, **52**, (6), pp. 4762–4769
- Taghavi, S., Pillay, P.: 'A comparative study of synchronous reluctance machine performance with different pole numbers for automotive applications'. In: IECOM 2014 - 40th Annual Conference of the IEEE Industrial Electronics Society. (IEEE, 2015, pp. 3812–3818)
- Vagati, A.: 'Ac motors for high-performance drives: A design-based comparison', *IEEE Trans Ind Appl*, 1996, **32**, (5), pp. 1211–1219
- Staton, D.A., Miller, T.J.E., Wood, S.E.: 'Maximising the saliency ratio of the synchronous reluctance motor', *Proc IEE—Elect Power Applicat*, 1993, **140**, (4), pp. 249–259
- Jiles, D.C., Atherton, D.L.: 'Theory of ferromagnetic hysteresis', *J Magn Magn Mater*, 1986, **61**, pp. 48–60
- Ma, M., Wu, Y., Zhou, J., Sun, Y., Zhang, Y., Gu, N.: 'Size dependence of specific power absorption of Fe₃O₄ particles in ac magnetic field', *J Magn Magn Mater*, 2004, **268**, pp. 33–39
- Jiles, D.C.: 'Modelling the effects of eddy current losses on frequency dependent hysteresis in electrically conducting media', *IEEE Trans Magn*, 1994, **30**, (6), pp. 48–60
- Shiozaki, M., Kurosaki, Y.: 'The effects of grain size on the magnetic properties of nonoriented electrical steel sheets', *J Magn Magn Mater*, 1989, **11**, (1), pp. 37–43
- de Campos, M.F., Teixeira, J.C., Landgraf, F.J.G.: 'The optimum grain size for minimizing energy losses in iron', *J Magn Magn Mater*, 2006, **301**, pp. 94–99
- de Campos, M.F., Yonamine, T., Fukuhara, M., Landgraf, F.J.G., Achete, C.A., Missell, F.P.: 'Effect of frequency on the iron losses of 0.5% and 1.5% Si nonoriented electrical steels', *IEEE Trans Magn*, 2006, **42**, (10), pp. 2812–2814
- Qin, J., Yang, P., Mao, W., Ye, F.: 'Effect of texture and grain size on the magnetic flux density and core loss of cold-rolled high silicon steel sheets', *J Magn Magn Mater*, 2015, **393**, pp. 537–543
- Pan, H., Zhang, Z., Xie, J.: 'The effects of recrystallization texture and grain size on magnetic properties of 6.5 wt% Si electrical steel', *J Magn Magn Mater*, 2016, **401**, pp. 625–632
- Jin, Y.M., Wang, Y.U., Kazayan, A., Wang, Y., Laughlin, D.E., Khachatryan, A.G.: 'Magnetic structure and hysteresis in hard magnetic nanocrystalline film: Computer simulation', *J Appl Phys*, 2002, **92**, (10), pp. 6172–6181
- Stephenson, E.T., Marder, A.R.: 'The effects of grain size on the core loss and permeability of motor lamination steel', *IEEE Trans Magn*, 1986, **MAG-22**, (2), pp. 537–543
- Herzer, G.: 'Nanocrystalline soft magnetic materials', *Physica Scripta*, 1993, **T49A**, (158), pp. 307–314
- Herzer, G.: 'Modern soft magnets: Amorphous and nanocrystalline materials', *Acta Mater*, 2013, **61**, pp. 718–734
- Ohta, M., Yoshizawa, Y.: 'Recent progress in high B_s Fe-based nanocrystalline soft magnetic alloys', *J Phys D: Appl Phys*, 2011, **44**, (6), pp. 064004
- Lashgari, H.R., Chu, D., Xie, S., Sun, H., Ferry, M., Li, S.: 'Composition dependence of the microstructure and soft magnetic properties of Fe-based amorphous/nanocrystalline alloys: A review study', *J Non-Cryst Solids*, 2014, **391**, pp. 61–82
- Makino, A.: 'Nanocrystalline soft magnetic Fe-Si-B-P-Cu Alloys With High B of 1.8-1.9T contributable to energy saving', *IEEE Trans Magn*, 2012, **48**, (4), pp. 1331–1335
- Knipling, K.E., Daniil, M., Willard, M.A.: 'Nanocrystalline Fe_{88-2x}Co_xNi_{2x}Zr₇B₄Cu₁ alloys: Soft magnets for vehicle electrification technologies (invited)', *J Appl Phys*, 2015, **117**, (17)
- Osaka, T., Takai, M., Hayashi, K., Ohashi, K., Saito, M., Yamada, K.: 'A soft magnetic CoNiFe film with high saturation magnetic flux density and low coercivity', *Nature*, 1998, **392**, (6678), pp. 796–798
- Kim, Y.M., Choi, D., Kim, S.R., Kim, K.H., Kim, J., Han, S.H., et al.: 'Magnetic properties of as-sputtered Co-Ni-Fe alloy films', *J Magn Magn Mater*, 2001, **226**, (230), pp. 1507–1509
- Suzuki, K., Parsons, R., Zang, B., Onodera, K., Kishimoto, H., Kato, A.: 'Copper-free nanocrystalline soft magnetic materials with high saturation magnetization comparable to that of Si steel', *Appl Phys Lett*, 2017, **110**, (012407), pp. 1–4
- Parsons, R., Zang, B., Onodera, K., Kishimoto, H., Kato, A., Suzuki, K.: 'Soft magnetic properties of rapidly-annealed nanocrystalline Fe-Nb-B-(Cu) alloys', *J Alloys Compd*, 2017, **723**, pp. 408–417
- Wang, F., Inoue, A., Han, Y., Zhu, S.L., Kong, F.L., Zanaeva, E., et al.: 'Soft magnetic Fe-Co-based amorphous alloys with extremely high saturation magnetization exceeding 1.9 T and low coercivity of 2 A/m', *J Alloys Compd*, 2017, **723**, pp. 376–384
- Vandevelde, L., Melkebeek, J.A.A.: 'Magnetic forces and magnetostriction in electrical machines and transformer cores', *IEEE Trans Magn*, 2003, **39**, (3), pp. 1618–1621
- Ghalamestani, S.G., Vandevelde, L., Melkebeek, J.A.A.: 'Magnetic forces and magnetostriction in rotating electrical machines', *Proc ICEM*, 2016, pp. 2287–2292
- Tanzer, T., Pregartner, H., Labinsky, R., Witlatschil, M.I., Muetze, A., Krischan, K.: 'Magnetostriction and its relation to the no-load noise of power transformers', *IEEE International Electric Machines and Drives Conference (IEMDC)*, 2017, pp. 7821–7823
- Masakatsu, K., Akira, S.: 'Effects of magnetostriction on electromagnetic motor vibration at sideband frequencies', *IEEE Trans Magn*, 2018, **54**, (2)
- Reddy, P.B., El-Refaie, A.M., Galioto, S., Alexander, J.P.: 'Design of synchronous reluctance motor utilizing dual-phase material for traction applications', *IEEE Trans Ind App*, 2017, **53**, (3), pp. 1948–1957
- Thottuvelil, V.J., Wilson, T.G., Owen, H.A.: 'High-frequency measurement techniques for magnetic cores', *IEEE Trans Power Electron*, 1990, **5**, (1), pp. 41–53
- 'Amorphous products catalog'. [Online; accessed July-2017]. <http://www.nanoamor.com/cat>
- 'Nonoriented electrical steel'. [Online; accessed July-2017]. <http://www.aksteel.com>
- 'Ohio supercomputer center'. 1987. [Online; accessed July-2017]. <http://osc.edu/ark:/19495/f5s1ph73>
- 'ANSYS Academic Research Electronics Desktop Help System'. (ANSYS, Inc, release 18.1)
- Lin, D., Zhou, P., Fu, W.N., Badcics, Z., Cendes, J.: 'A dynamic core loss model for soft ferromagnetic and power ferrite materials in transient finite element analysis', *IEEE Trans Magn*, 2004, **40**, (2), pp. 1318–1321
- Krings, A., Soulard, J.: 'Overview and comparison of iron loss models for electrical machines', *J Electr Eng*, 2010, **10**, (3), pp. 1162–169
- Bertotti, G.: 'Physical interpretation of eddy current losses in ferromagnetic materials. i. theoretical considerations', *J Appl Phys*, 1985, **57**, (6), pp. 2110–2117
- Bertotti, G.: 'Physical interpretation of eddy current losses in ferromagnetic materials. ii. analysis of experimental results', *J Appl Phys*, 1985, **57**, (6), pp. 2118–2126
- Tekgun, B.: 'Analysis, Measurement and Estimation of the Core Losses in Electrical Machines'. PhD Thesis, University of Akron, Akron, OH, 2016
- Tekgun, B.: 'Core loss estimation in electric machines with flux-controlled core loss tester', *IEEE Trans Ind Appl*, 2019, **55**, (2), pp. 1299–1308

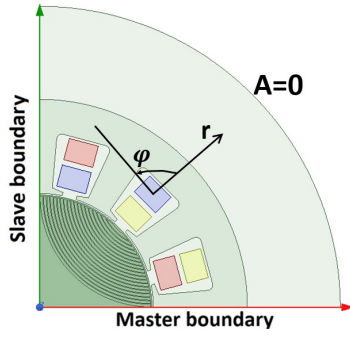


Fig. 14: Boundary conditions of the problem domain.

7 Appendices

7.1 FEA software setup

FEA software magnetostatic transient solver [37] is utilized to simulate electromagnetic fields in electrical machines. For the simulation, the following equation is solved

$$\nabla \times \left(\frac{1}{\mu} \nabla \times \mathbf{A} \right) = \mathbf{J} - \sigma \frac{\partial \mathbf{A}}{\partial t} \quad (8)$$

where \mathbf{A} is the magnetic vector potential, \mathbf{J} is the total current density vector, μ is the magnetic permeability, and σ is the electric conductivity. The current density \mathbf{J} is proportional to the applied stator winding current and is assumed to be uniformly distributed within the stator winding. The current density vector and the magnetic vector potentials are normal to the xy plane. Once the vector potential has been computed, the magnetic flux density is obtained using $\mathbf{B} = \nabla \times \mathbf{A}$.

The computational domain is discretized automatically into triangular surface elements with six nodes (3 corners and 3 midpoints). The magnetic vector potential inside the triangles is calculated using a second order quadratic interpolation scheme.

Figure 14 shows the boundary conditions of the proposed SyncRM. Master and slave boundaries are used to model planes of periodicity on the left and bottom boundaries of the problem domain, respectively. The H-field at every point on the slave boundary surface is forced to match the H-field of every corresponding point on the master boundary surface. Zero vector potential is also assigned on the outer radial boundary.

To model the anisotropy of the MWs, the material properties are defined in respect to a cylindrical coordinate system fixed to the rotor as shown in figure 14; r and φ are the radial and tangential directions, respectively.

7.2 Core loss calculation in numerical simulation

The instantaneous core loss is obtained as the sum of hysteresis, eddy current, and excess losses [38]:

$$P_{\text{tot}} = \frac{K_{\text{hys}}}{\pi} \sqrt{(B_{\text{max}} - B)} \left(\left| \frac{dB_r(t)}{dt} \right| + \left| \frac{dB_\varphi(t)}{dt} \right| \right) + \frac{K_{\text{edd}}}{2\pi^2} \left(\left| \frac{dB_r(t)}{dt} \right|^2 + \left| \frac{dB_\varphi(t)}{dt} \right|^2 \right) + \frac{K_{\text{exc}}}{8.76} \left(\left| \frac{dB_r(t)}{dt} \right|^2 + \left| \frac{dB_\varphi(t)}{dt} \right|^2 \right)^{0.75} \quad (9)$$

where B_{max} is the maximum of magnetic flux density, B is the absolute value of the flux density, and K_{hys} , K_{edd} , and K_{exc} are hysteresis, eddy current, and excess core loss coefficients, respectively, which depend on the material. In the proposed rotor, the anisotropy property of the material is introduced through the permeability tensor. Based on the core losses presented in figure 3(b), the $K_{\text{hys}} = 18$

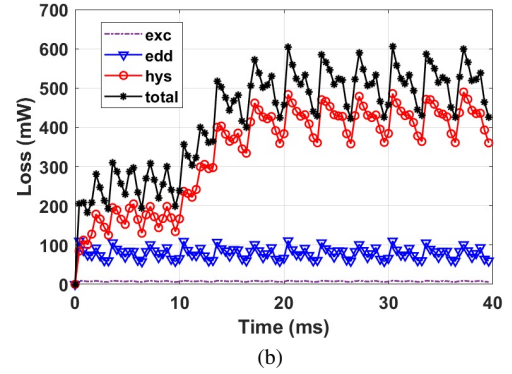
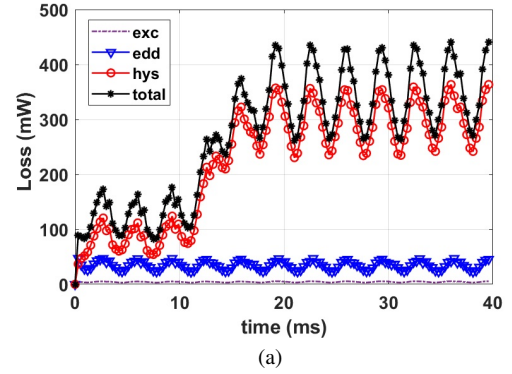


Fig. 15: a) Numerical results of the core loss (stator + rotor) in the a) MW-based and b) conventional SyncRM. The figure shows total core (black curve), hysteresis (red curve), eddy current (blue curve), and excess (purple curve) losses. Frequency is 50 Hz.

$\frac{W \cdot s}{m^3 \cdot T^2}$ and $K_{\text{edd}} = 0.0177 \frac{W \cdot s^2}{m^3 \cdot T^2}$, and $K_{\text{exc}} = 0.01 \frac{W \cdot s^{1.5}}{m^3 \cdot T^{1.5}}$ coefficients are obtained and used in SyncRM numerical analysis to calculate the core loss. Figures R4 and R5 show the total core losses (i.e. stator and rotor) of the MW-based SyncRM and conventional SyncRM, respectively. As seen, the proposed rotor represents lower total core loss compared with the conventional SyncRM.

Figures 15(a) and 15(b) present the total stator and rotor core losses of the MW-based and conventional SyncRM at 1500 rpm, respectively. The average total losses of the MW-based and conventional SyncRM are 360 mW and 510 mW, respectively.

7.3 Loss estimation*

Loss estimation and measurement in magnetic cores is known to be quite a complicated subject. Based on the loss separation method, the core loss is split into hysteresis losses and dynamic eddy current losses. The method has good accuracy for some Nickel-Iron alloys but poor accuracy for Silicon-Iron alloys [39]. The loss separation method was further improved by incorporating an additional term, called excess or anomalous loss component that depends on empirical factors including the physical description of the active magnetic objects and the domain wall motion [40–42]:

$$P_{\text{core}} = K_{\text{hys}} f B^{1.6} + K_{\text{edd}} f^2 B^2 + K_{\text{exc}} f^{1.5} B^{1.5} \quad (10)$$

Since loss separation models are approximate, we have developed a methodology [42, 43] that combines simulations and measurements and allows us to determine the losses with a higher level of accuracy than would be possible with other published methods. First, FEM simulations are used to find fields at different locations in the

*This appendix is included at the suggestion of one of the anonymous reviewers; we thank him/her for the comments.

machine. Second, loss measurements are performed on core samples that are subject to these field values. Detailed information can be found in [42, 43].